# Equilibration of a Simple Baroclinic Flow in a $\beta$ Channel and on the Sphere

RODRIGO CABALLERO

*Danish Center for Earth System Science, University of Copenhagen, Copenhagen, Denmark*

ALFONSO SUTERA

*Dipartimento di Fisica, Università di Roma "La Sapienza," Rome, Italy*

(Manuscript received 16 October 1998, in final form 2 February 2000)

ABSTRACT

The statistical equilibration of baroclinic waves in a two-level quasigeostrophic model subject to forcing and dissipation is studied. The model employed may be formulated in either spherical or Cartesian geometry and is restricted to a midlatitude channel. Parameters are chosen so that only up to three waves can become supercritical (one planetary- and two synoptic-scale waves). It is found that both geometries exhibit essentially two equilibration regimes as the forcing temperature gradient varies. At low forcing, the planetary-scale wave is not excited while the two synoptic-scale waves equilibrate with steady finite amplitude. In this regime, the equilibrated temperature gradient is sensitive to forcing; the authors argue that this is due to the barotropic governor effect. At higher forcing, the planetary wave becomes active and the solution is aperiodic. In this regime, the planetary wave acts to reduce the barotropic shear spun up by the synoptic waves, thereby limiting the role of the barotropic governor; the equilibrated temperature gradient then becomes much less sensitive to forcing. The Cartesian and spherical cases differ both in the structure of the equilibrated state and in the strength of the barotropic governor (which is greater on the sphere). These differences are related to the geometric curvature terms and not to the meridional variation of $\beta$.

## 1. Introduction

Climate is by definition the collection of long-term statistics of all relevant geophysical variables. A central theme in climate research is the search for closure or parameterization schemes whereby the net effect of small-scale, short-lived disturbances may be expressed as a function of the climatologically averaged variables themselves. An example of such parameterization is convective adjustment theory (Manabe and Strickler 1964), whereby the statistical effect of small-scale convective processes is described in terms of macroscopic variables such as the tropospheric lapse rate. Much effort has been devoted to the development of an analogous scheme for the statistical effect of baroclinic eddies on the general circulation of the atmosphere. Indeed, convectively adjusted radiative balance leaves the atmosphere in a state (which, following common usage, we refer to as the "Hadley state," though a Hadley cell is not necessarily present) that can be supercritical with respect to baroclinic instability. The resulting eddies will transport heat and momentum both horizontally and vertically. Plausibly, these transports will, on timescales proper for the climatic state, leave the system in a "baroclinically adjusted" state that is close to neutrality.

Of course, invoking neutrality is not the only way of obtaining an eddy parameterization. For instance, the eddies may be modeled as a diffusive process (Held 1999). However, the assumption of neutrality is appealing in view of the theorem due to Charney and Stern (1962). The theorem states that a given zonally symmetric flow is stable if the meridional gradient of quasigeostrophic potential vorticity,

$$\partial_y q = \beta - \partial_{yy} u - \frac{1}{\rho}\partial_z \frac{\rho f_0^2}{N^2}\partial_z u - \frac{f_0^2}{N^2}\partial_z u \delta(z - 0), \quad (1)$$

has uniform sign throughout the fluid [here, the $\beta$-plane assumption is made for simplicity; $\partial_{(\cdot)}$ indicates a partial derivative with respect to $(\cdot)$, while $q$ is the quasigeostrophic potential vorticity, $u$ is the zonal wind, $\delta$ is the density, $f_0$ is the Coriolis parameter, and $N$ is the Brunt–Väisällä frequency]. This is only a sufficient condition, but in practice flows in which $\partial_y q$ changes sign are generally found to be unstable. Thus, the neutrality assumption gives a clear prescription for the effect of eddies on the Hadley state: they will simply wipe out sign changes in $\partial_y q$.

*Corresponding author address:* Dr. Rodrigo Caballero, Danish Center for Earth System Science, University of Copenhagen, Juliane Maries Vej 30, DK-2100 Copenhagen Ø, Denmark.
E-mail: rca@dcess.ku.dk

The problem then is to determine which of the terms on the rhs of (1) dominates the adjustment. For the sake of argument, let us make two assumptions:

1) Two-level dynamics is relevant; and
2) the eddies have a negligible effect on both the static stability and the meridional structure of the flow.

Assumption (ii) implies that the eddies can only act on $\partial_y q$ through the vertical wind shear (or, equivalently, the horizontal temperature gradient). In a two-level model, it is easily shown that sign changes in $\partial_y q$ will be eliminated when the temperature gradient falls below a certain critical value. We thus have a very simple eddy parameterization: the only effect of the eddies is to reduce the temperature gradient down to its critical value (which is easy to compute given the Hadley state). This form of baroclinic adjustment, which we will refer to as ''strict baroclinic adjustment,'' was advocated by Stone (1978), who showed evidence that the temperature gradient observed in the real atmosphere is actually close to (two level) criticality and depends little on seasonality. Further, if a single wave with no meridional tilt is allowed to equilibrate in a two-level model, then strict baroclinic adjustment is exact (Pedlosky 1970; Vallis 1988).

Unfortunately, baroclinic adjustment is confronted by a number of problems. For one thing, a vertically continuous atmosphere does not have a critical temperature gradient. We may get around this problem by assuming that the heat flux is dominated by deep troposphere-filling eddies (Held 1978) that are only excited when the temperature gradient exceeds a certain threshold. However, even in a two-level model, the adjusted state is generally found to be supercritical if many zonal and meridional waves are allowed to intervene in the equilibration (Salmon 1980; Vallis 1988; Stone and Branscome 1992). An extended form of baroclinic adjustment that accounts for this difficulty was proposed in a series of papers by Cehelsky and Tung (1991), Welch and Tung (1998a, hereafter WT), and Welch and Tung (1998b). They found that baroclinic waves appear unable to grow beyond a given amplitude without breaking. This sets an upper limit on a given wave's heat transport. Since lower wavenumbers turn out to have higher-amplitude thresholds, the result is that as the level of forcing rises, the shorter waves saturate and the burden of heat transport is shifted to ever longer waves. They use this finding to introduce the concept of ''nonlinear baroclinic adjustment,'' whereby the temperature gradient is adjusted so as to be neutral with respect to the *main heat carrying wave,* while it may remain supercritical with respect to *shorter waves.* If assumptions (i) and (ii) above continue to hold (''strict nonlinear baroclinic adjustment''), and if we know which wave dominates the heat transport, we are again led to a simple eddy parameterization.

We note also that Lindzen (1993) has proposed a neutralization mechanism that does not rely on the Charney–Stern theorem. Assuming potential vorticity (PV) to be horizontally well mixed, so that the atmosphere is close to an Eady state, and assuming the eddies are meridionally confined by the barotropic jet, then by suitably adjusting the height of the upper boundary all normal modes will have wavenumbers higher than the short-wave cutoff. However, some general circulation model (GCM) simulations by Thuburn and Craig (1997) appear not to confirm the hypothesis. The discrepancy may lie in the fact that the Eady model has a rigid upper boundary, which does not exist in the real atmosphere (or in a GCM). An extension of Lindzen's mechanism to an Eady model with a nonrigid tropopause is discussed in Bordi and Sutera (1998).

We emphasize that, in order for baroclinic adjustment theories to provide a useful parameterization, it is crucial that we are able to predict the equilibrated temperature gradient quite accurately. This is not a problem, of course, if strict baroclinic adjustment is a good approximation. However, there are grounds for thinking that in general it will not be so. Indeed, the Eliassen–Palm theorem states that, in an inviscid unforced flow, the eddies leave the zonal-mean flow unmodified (Edmon et al. 1980). Baroclinic adjustment implies that the Eliassen–Palm theorem is strongly violated by forcing and dissipation—otherwise there could be no adjustment of the temperature gradient. Thus there is little reason to assume that the meridional wind shear and vertical temperature gradient will not be affected as well.

In the present study, we hold the static stability fixed and focus on changes in the meridional structure of the flow [the adjustment of $N$ has been studied by Gutowski (1985) and references therein]. This issue is of some concern since it is well known that, in the decaying phase of a baroclinic life cycle, a meridionally sheared barotropic component is added to the zonal-mean flow (Simmons and Hoskins 1978; Randel and Stanford 1985b). The effect of this barotropic shear is generally to raise the critical temperature gradient (James 1987), an effect known as the ''barotropic governor'' (James and Gray 1986; Nakamura 1993). Thus, while baroclinic adjustment may continue to apply (in the sense that the temperature gradient is adjusted so as to render the flow neutral), we are unable to predict the equilibrated temperature gradient, since there is currently no theory telling us how much shear is added and how far the critical gradient is raised.

Our aim in this study is twofold. First, we examine the statistics of a simple two-level model and assess the accuracy with which strict baroclinic adjustment predicts the equilibrated temperature gradient. It has been shown (Whitaker and Snyder 1993; Nakamura 1993; Balasubramanian and Garner 1997; Dong and James 1997) that the earth's sphericity can significantly affect baroclinic life cycles, so the study is conducted in parallel in both Cartesian and spherical geometry. As it turns out, significant deviations from strict baroclinic

adjustment are found, particularly in the spherical case. Our second aim is to examine the dynamical nature of the equilibration and attempt to account for such discrepancies. We note that our study employs a single parameter setting and contains many limiting assumptions (quasigeostrophy, channel geometry, rigid lid, no topography, etc.). Strict baroclinic adjustment may hold more accurately when some of the limiting assumptions are relaxed. We leave this question to future work; our aim here is to gain physical insight into the equilibration process and to point out some of the issues to bear in mind when studying more realistic models.

The layout of the study is as follows. The model we use is presented in section 2. In section 3 we study the Hadley state and its stability. The model's climatology is studied and baroclinic adjustment assessed in section 4. In section 5 we describe the equilibration scenarios in our model as forcing is varied. Our results are summarized in section 6.

## 2. Model

### a. Equations of motion

We employ the simplest among the hierarchy of two-level models proposed by Lorenz (1960), which is also known as the B model (Baines and Frederiksen 1978):

$$\partial_t \nabla^2 \psi = -J(\psi, \nabla^2\psi + f) - J(\tau, \nabla^2\tau) - \frac{\nu_E}{2}\nabla^2(\psi - \tau) + \nu_d \nabla^4 \psi \quad (2)$$

$$\partial_t \nabla^2 \tau = -J(\tau, \nabla^2\psi + f) - J(\psi, \nabla^2\tau) + \frac{\nu_E}{2}\nabla^2(\psi - \tau) + \nu_d \nabla^4 \tau + f_0 \omega \quad (3)$$

$$\partial_t \theta = -J(\psi, \theta) + \sigma\omega - \nu_h(\theta - \theta^*) \quad (4)$$

$$\theta = \frac{f_0}{bC_p}\tau. \quad (5)$$

In spherical coordinates, we have

$$J(a, b) = \frac{1}{r^2 \cos\varphi}(\partial_\lambda a \partial_\varphi b - \partial_\lambda b \partial_\varphi a) \quad (6)$$

$$\nabla^2 a = \frac{1}{r^2 \cos^2\varphi}(\cos\varphi \partial_\varphi(\cos\varphi \partial_\varphi a) + \partial_\lambda^2 a), \quad (7)$$

where $r$ is the earth's radius, $\varphi$ is latitude, $\lambda$ is longitude, and $\partial_{(\cdot)}$ represents the partial derivative with respect to $(\cdot)$. The model variables are the barotropic streamfunction $\psi = (\psi_1 + \psi_2)/2$, the baroclinic streamfunction $\tau = (\psi_1 - \psi_2)/2$, the vertically averaged potential temperature $\theta = (\theta_1 + \theta_2)/2$, and the vertical velocity midway between the two levels $\omega$ (indexes 1 and 2 indicate the upper and lower level, respectively). The fixed static stability is represented though the constant $\sigma = \theta_1 - \theta_2$, which is taken as a climatological value of the potential temperature difference between the upper and lower troposphere. The Coriolis parameter $f = 2\Omega \sin\varphi$ is allowed to vary in the advective terms but is held fixed at the value $f_0$ in the vortex stretching terms to ensure energy conservation (Mak 1991). Further, $b$ is a dimensionless constant arising from the vertical discretization and $C_p$ is the specific heat of air at constant pressure. The model includes Ekman damping in the lower level with time constant $\nu_E$ and a biharmonic dissipation term with coefficient $\nu_d$ in both levels. Diabatic heating is simply modeled through linear relaxation toward a prescribed zonally symmetric temperature profile $\theta^*$ with time constant $\nu_h$.

### b. Numerical implementation, geometry, and parameter values

For purposes of numerical integration, the equations may be rewritten in a more concise form by using (4) and (5) to eliminate the vertical velocity in (3), giving the standard two-level quasigeostrophic system:

$$\partial_t \nabla^2 \psi = \frac{\beta}{r\cos\varphi}\partial_\lambda \psi - J(\psi, \nabla^2\psi) - J(\tau, \nabla^2\tau) - \frac{\nu_E}{2}\nabla^2(\psi - \tau) + \nu_d \nabla^4 \psi \quad (8)$$

$$\partial_t(\nabla^2 - 2F)\tau = \frac{\beta}{r\cos\varphi}\partial_\lambda \tau - J(\tau, \nabla^2\psi) - J(\psi, \nabla^2\tau) + 2FJ(\psi, \tau) + \frac{\nu_E}{2}\nabla^2(\psi - \tau) + \nu_d \nabla^4 \tau + 2F\nu_h(\tau - \tau^*), \quad (9)$$

where we explicitly display the beta parameter $\beta = 2\Omega r^{-1} \cos\varphi$. Here $F = f_0^2(2bC_p\sigma)^{-1}$ is the rotational Froude number, and $\tau^*$ is obtained from $\theta^*$ through (5).

Examination of (6)–(9) shows that the curvature of the earth's surface is reflected only in the presence of $\cos\varphi$ in the equations. Thus we may switch to Cartesian geometry by simply setting $\cos\varphi = const.$ everywhere. This allows us to assess the effects of curvature consistently, employing a single numerical scheme. Specifically, we refer in what follows to the three following model configurations ($\varphi_0$ is the latitude at channel center):

- Cartesian model (CM): $\cos\varphi = \cos\varphi_0$ everywhere in (6)–(9);
- Variable $\beta$ model (VBM): $\cos\varphi = \cos\varphi_0$ everywhere in (6)–(9) except in $\beta$: the geometry is Cartesian, but latitudinal variation is retained in $\beta$; and
- Spherical model (SM): full sphericity retained in (6)–(9).

The numerical scheme we employ is spectral in the zonal direction but grid point in the meridional, which makes it easy to switch between Cartesian and spherical geometry and to confine the model domain to a mid-

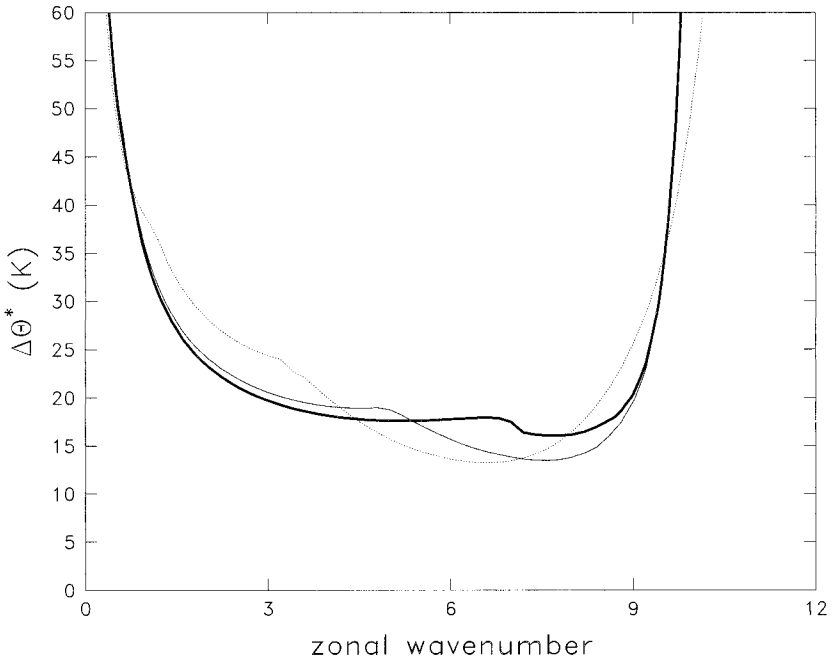


FIG. 1. Hadley state marginal stability curves for the CM (thick solid line), VBM (thin solid line), and SM (dotted line).

latitude channel. All runs in this study employ a channel of 45° latitudinal extent, centered at 40°N. To restrict the number of active waves in the simulations, we include only zonal wavenumbers that are integer multiples of 3 (equivalent to employing a channel of length equal to one-third the earth's circumference). In all runs we employ a resolution of 20 zonal wavenumbers (so that the smallest wave has wavenumber 60) and 30 grid points in latitude. The eddy amplitudes and the zonal-mean wind are zero at the channel boundaries at all times (so that the channel is bounded by solid walls; Phillips 1954).

We have verified our numerical scheme, in the SM case, by comparing its output to that of an independently coded, fully spectral scheme, obtaining excellent agreement. We have also run the Cartesian version of the model using the parameter setting specified in WT, again obtaining good agreement with the statistics presented in that paper.

In all three model configurations, $\theta$ is linearly related to the baroclinic streamfunction $\tau$ through the "thermal wind relation" (5); we take the numerical values of the constants in this relation as $f_0 = 10^{-4}$ s$^{-1}$, $b = 0.124$ and $C_p = 1004$ J K$^{-1}$ kg$^{-1}$. Throughout the study we fix the values of the constants in (8) and (9) to be $F = 2 \times 10^{-12}$ m$^{-2}$ (implying a potential temperature difference of 20 K between the two levels, somewhat smaller than the 30 K difference between the upper and lower troposphere typically observed in midlatitudes), $\nu_E = 0.18 \times 10^{-5}$ s$^{-1}$ (6.4 day Ekman damping time), $\nu_d = 0.01 \times 10^7$ m$^2$ s$^{-1}$. We motivate this choice of parameter settings in the following section. Following WT, we set $\nu_h = 0.02 \times 10^{-5}$ s$^{-1}$ (58 day cooling time).

## 3. The Hadley state and its stability

We use a cosine-shaped profile for the diabatic heating. Specifically, we put

$$\theta^*(\varphi) = \theta^*(\varphi_1) + \frac{\Delta\theta^*}{2}\left(\cos\left(\frac{\varphi - \varphi_1}{\varphi_2 - \varphi_1}\pi\right) - 1\right), \quad (10)$$

where $\varphi_1$ and $\varphi_2$ are the latitudes of the equatorward and poleward channel boundaries, respectively, while $\Delta\theta^*$ is the temperature drop across the channel.

In the absence of eddies, examination of (8), (9) (noting that we allow the diffusion term proportional to $\nu_d$ to act only on the eddy part of the flow) shows that there is an equilibrium solution (the Hadley state) given by $\psi^{\text{Hadley}} = \tau^{\text{Hadley}} = \tau^*$. The corresponding zonal winds in the upper and lower level are

$$u_1^{\text{Hadley}} = U_1 \sin\left(\frac{\varphi - \varphi_1}{\varphi_2 - \varphi_1}\pi\right) \qquad u_2^{\text{Hadley}} = 0,$$

representing a sine-shaped upper level jet that is zero at the boundaries and has maximum intensity $U_1 = \pi\Delta\theta^* bC_p[f_0 r(\varphi_2 - \varphi_1)]^{-1}$ at the center of the channel. This solution is valid for all three model configurations. Note that this Hadley state actually contains no Hadley cell, as there is no vertical viscosity.

The stability of the Hadley state as a function of $\Delta\theta^*$ in the three models is studied in Fig. 1. Growth rates

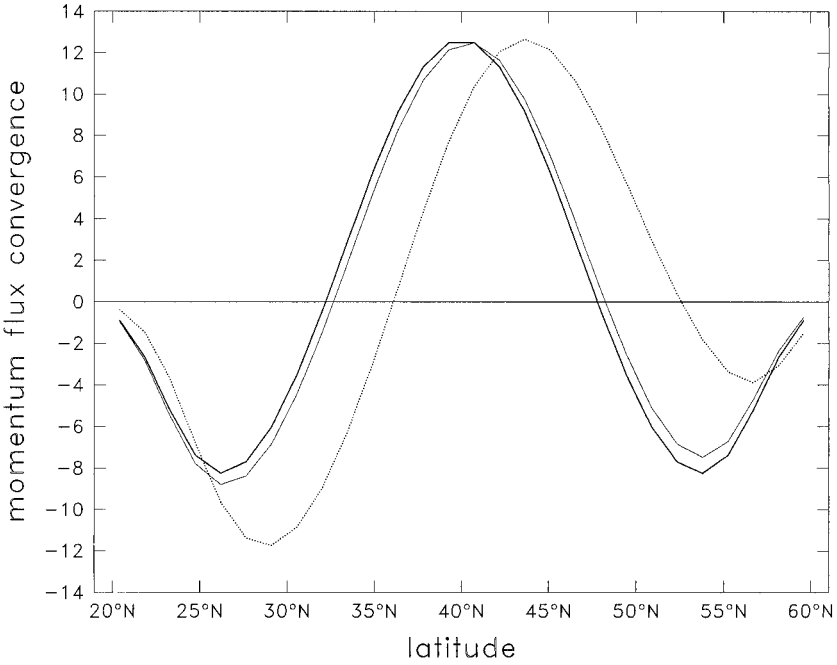


FIG. 2. Upper-layer momentum flux convergence of the most unstable mode of the Hadley state at $\Delta\theta^* = 80$ K, zonal wavenumber 6, for the CM (thick solid line), VBM (thin solid line), and SM (dotted line). Units are arbitrary.

have been computed by linearizing the equations of motion around the Hadley state (using the same numerical scheme and resolution employed in the time-dependent model) and then diagonalizing the resulting Jacobian matrix. With our choice of parameters, only three waves (3, 6, and 9) can become unstable up to $\Delta\theta^* = 500$ K. The instability thresholds (or critical gradients) for waves (3, 6, 9) are (19.5, 18, 21), (21, 16, 19.5), and (24.5, 14, 25.5) for the CM, VBM, and SM, respectively. Wave 6 is the most unstable at all forcings in all models.

To study multiwave equilibration in the simplest context, it might have been preferable to have only two unstable waves (3 and 6). As it turns out, it is not easy to achieve this in the SM while keeping wave 6 as the most unstable wave; some experimentation within a realistic parameter range showed that wave 3 was the most unstable in situations with only two unstable waves (while it was generally still 6 in the CM). The parameter setting we have chosen seems a good compromise. As it turns out, the presence of wave 9 does not complicate analysis greatly.

As Fig. 1 shows, sphericity does have some effect on the stability of the waves, introducing changes of up to 5 K in the critical gradients and widening the gap between the critical gradients of waves 3 and 6. However, as we will see later, the momentum and heat flux convergences of the growing waves generally change the shape of the zonal-mean flow quite drastically, and we therefore do not expect the detailed stability characteristics of the Hadley state to have much relevance for the finite-amplitude equilibration. More crucial to the dynamics is the effect of sphericity on the structure of the normal modes' momentum fluxes. Figure 2 shows an example (taken at $\Delta\theta^* = 80$ K; plots at other values of $\Delta\theta^*$ have the same qualitative features). While the flux convergence is exactly symmetric around the channel center in the CM, and nearly so in the VBM, there is a clear northward bias in the SM. We will examine the way this asymmetry influences equilibration in the following sections.

## 4. Statistics in the equilibrated state

In this section we address the issue of baroclinic adjustment in the context of the present models' climatology. To this end, we present results of a series of model runs in which the geometry and parameters were fixed at the values stated above, while the forcing temperature $\Delta\theta^*$ was varied from small to very large supercriticality. As it turns out, at high forcing the time-average wave amplitudes become so large (on the order of several kilometers of geopotential height) that the assumptions under which the models were derived cannot be expected to hold; in particular, we would expect vertical heat transports to strongly modify the static stability. Thus we will focus on the behavior below $\Delta\theta^* = 160$ K, though we actually carried out runs up to 500 K. Each run started with the Hadley state plus a small randomly chosen perturbation on each wave (the same initial perturbation was used in all runs). All runs lasted for 2000 days and data were sampled once daily. Except at very low forcings, a statistically steady state (the

''equilibrated state'') was reached within 150 days or less. Statistics are taken over the last 1800 days of each run.

In this and the remaining sections of the paper we will only discuss the CM and SM. This is because the VBM produces results that are essentially identical to those of the CM. This implies that all differences noted between the CM and SM must be attributed to the geometric curvature terms, rather than to the meridional variation of $\beta$.

The first question to address is, does baroclinic adjustment apply? In other words, is the mean state adjusted so as to be neutral (or stable)? To answer this question, we simply compute the stability of the time- and zonally averaged equilibrated state.[1] Results are shown in Figs. 3a,b. In both geometries, the equilibrated state is close to neutrality (or stable) up to around $\Delta\theta^* = 40$ K, but at higher forcing it becomes unstable to wave 6, with *e*-folding times averaging 20 days (10 days) in the CM (SM). Thus, as found in previous studies (Salmon 1980; Vallis 1988; Stone and Branscome 1992; WT), ordinary baroclinic adjustment does not apply when forcing is high.

Can we account for this supercritical equilibration at high forcing in terms of nonlinear baroclinic adjustment? This requires the equilibrated state to be stable with respect to the wave that dominates the heat transport. The heat flux for waves 3–9 is plotted as a function of forcing in Figs. 3c,d. In the CM, wave 6 dominates the heat flux at all forcings higher than 50 K. In the SM, wave 6 is clearly dominant only up to $\Delta\theta^* = 80$ K, when wave 3 begins to play an increasing role. As we saw above, wave 6 is unstable for $\Delta\theta^*$ greater than 50 K in both CM and SM. If we wished to be strict, we would conclude that nonlinear baroclinic adjustment is not operative. On the other hand, this conclusion is perhaps unfair. In the CM, growth rates are actually quite small, and there is a significant minimum between $\Delta\theta^* = 70$ and 160 K, with the system becoming neutral at $\Delta\theta^* = 100$ K. In the SM, the range in which wave 6 is *clearly* the dominant wave is quite narrow; after $\Delta\theta^* = 80$ K, the situation resembles one of the ''transition regimes'' described by WT. Overall, our simulations do not give strong evidence either for or against the nonlinear baroclinic adjustment hypothesis.

In any case, let us heuristically assume that nonlinear baroclinic adjustment *is* operative in our model, and ask the further question, is *strict* baroclinic adjustment a good approximation? Here the answer is more clear-cut. In Figs. 3e,f we plot the equilibrated temperature gradient $\Delta\theta_e$ (defined as the time- and space-averaged meridional temperature gradient in the equilibrated state) as a function of $\Delta\theta^*$. Also plotted (thin solid line) is a sketch of what the $\Delta\theta_e$ curve might look like if strict nonlinear baroclinic adjustment were exact. In the CM, the difference between the two curves is on average about 5 K (25%–30% relative error). The difference in the SM is higher, averaging more than 10 K (50%–60% relative error). Strict baroclinic adjustment is clearly not a good approximation, especially in the SM.

A cursory examination of the structure of the equilibrated flow gives some motivation for the observed deviations from strict baroclinic adjustment. In Fig. 4 we plot the time-mean barotropic component of the zonal wind. Generally, the structure is quite different from the broad, meridionally symmetric jet present in the Hadley state. Rather, the jet is narrow and compressed against the northern channel wall (sometimes the southern wall in the CM). The region beyond $\Delta\theta^* = 80$ K in the CM appears to be an exception; in fact, as we discuss in more detail below (section 5b), what happens here is that the jet oscillates between northern- and southern-confined configurations, so that the time mean is approximately meridionally symmetric; however, this mean does not represent a typical jet configuration.

The barotropic shear in the equilibrated state is higher than in the Hadley state, suggesting that the barotropic governor is in action. Also, the barotropic jet is more intense in the SM than in the CM, so we expect a more important role for the barotropic governor in the former. More evidence in this direction is found when examining the model energetics, shown in Fig. 5. Note that both the available potential energy (APE) and kinetic energy (KE) of the zonal-mean flow (Figs. 5a,b) are higher in the SM than in the CM (consistent with the higher $\Delta\theta_e$ and stronger barotropic jet observed in the former). Vice versa, the total eddy energy is lower in the SM. The combination of higher zonal energies and lower eddy energies is the typical signature of an enhanced the barotropic governor (James and Gray 1986). Further, the ratio of net barotropic to net baroclinic energy conversion (Figs. 5c,d) is generally higher in the SM, which is again consistent with an enhanced barotropic governor.

## 5. Equilibration regimes

In the present section we examine the dynamics of the equilibration and attempt to give some motivation for the behavior of the statistics described in the previous section. To guide the reader through this rather lengthy section, we present here a brief summary.

In both CM and SM, there are essentially two equilibration regimes, one at low and one at high forcing. We call them respectively C-I and C-II in the CM (S-I and S-II in the SM). Approximate regime boundaries

[1] An alternative approach is to write the time- and zonal-average equilibrated state as $U_B B(\varphi)$, $U_b b(\varphi)$, where $U_B$ and $U_b$, respectively, give the magnitude of the barotropic and baroclinic zonal-mean wind while $B$, $b$ are normalized functions giving the meridional structure. One can then hold $U_B$ fixed and vary $U_b$ until an exactly neutral state is found. This gives the ''critical gradient of the equilibrated flow.'' Note, however, that this state is unphysical since $U_B$ is arbitrarily held constant. Changing $U_B$ would strongly affect the stability. We therefore prefer the direct approach used here.

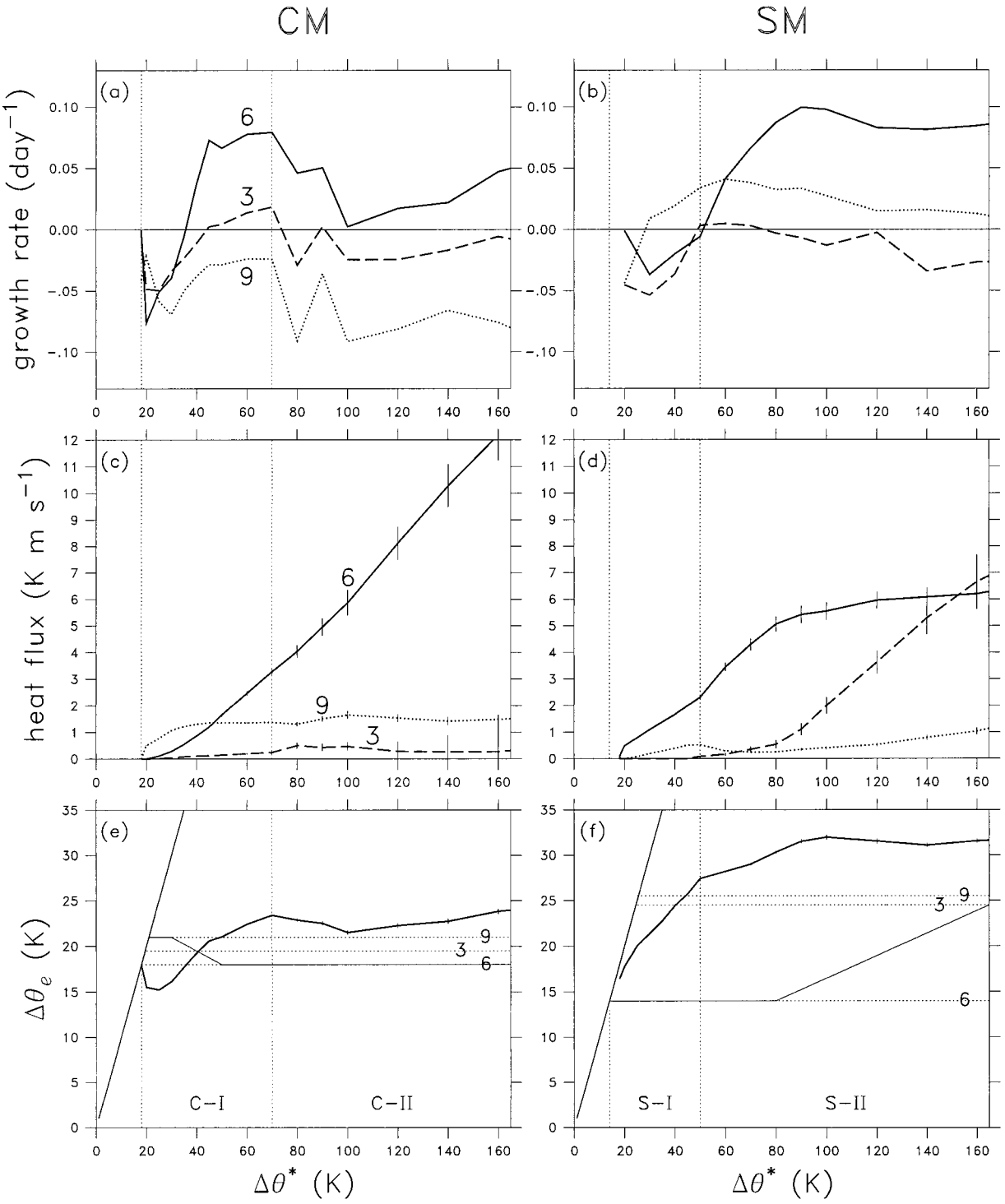


FIG. 3. Some statistics of the equilibrated state as a function of $\Delta\theta^*$ in the CM (left-hand column) and SM (right-hand column). Top row: most unstable mode growth rates of the time- and zonal-mean flow. Middle row: heat flux. Bottom row: mean temperature gradient $\Delta\theta_e$. In (a)–(d) results are shown only for waves 3 (dashed line), 6 (solid line), and 9 (dotted line). In (e) and (f), the diagonal line indicates the Hadley state; the dotted horizontal lines indicate the critical gradients in the Hadley state for wave 3 (middle), 6 (lower) and 9 (upper); while the vertical dotted lines indicate regime boundaries; the regimes are labeled along the bottom of the panels. A sketch of the $\Delta\theta_e$ as it would appear in the strict nonlinear baroclinic adjustment hypothesis is shown by the thin solid line. In (c)–(f), statistical uncertainty in the estimates is indicated by vertical bars of length $2 \times \sqrt{\sigma^2/N}$, where $\sigma^2$ is the sample variance and $N$ is the sample length divided by the decorrelation time. A decorrelation time of 2 days is assumed; this is an underestimate at low forcing but is not severe since the variance there is small. The bars are always plotted but are often too short to be visible.

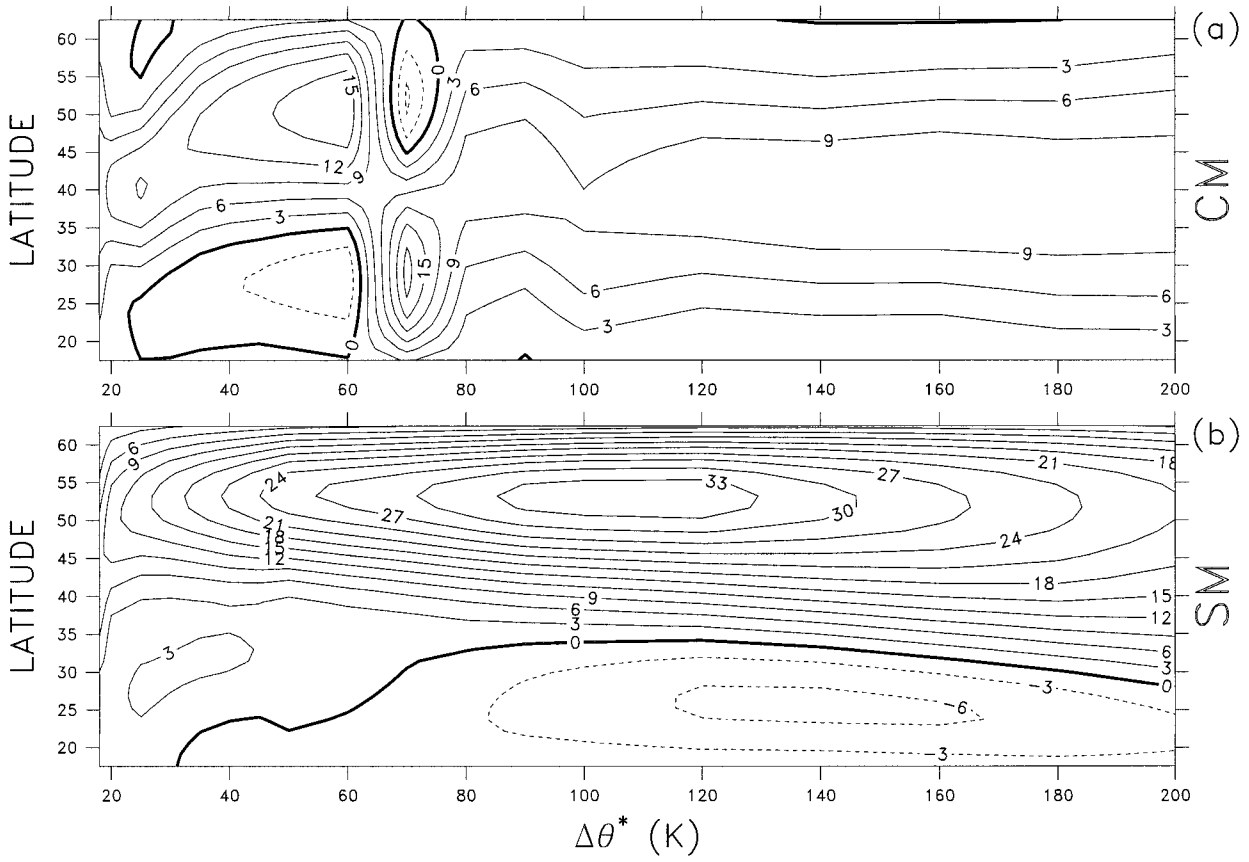


FIG. 4. Time-mean barotropic component of the zonal-mean wind in the equilibrated state as a function of $\Delta\theta^*$ in (a) the CM and (b) the SM. Contour interval is 3 m $s^{-1}$. Zero contour is darkened and negative contours dashed.

are shown by dotted vertical lines in Fig. 3. The CM regimes are of essentially the same nature as the respective SM regimes, though there are some important differences.

Features common to both CM and SM are as follows. In the low-forcing regime, the equilibrated state is a stable solution in which the two synoptic-scale waves (6 and 9) have steady finite amplitude. The waves maintain themselves through baroclinic conversion (Figs. 5g–j), so $\Delta\theta_e$ is always lower than $\Delta\theta^*$. The waves also return some energy back to the zonal-mean flow as KE, strengthening the barotropic jet and thus reducing the efficiency with which they can extract APE (this is the essence of the barotropic governor effect). The equilibrated temperature gradient results from this delicate nonlinear balance. As it turns out, the balance is such as to render $\Delta\theta_e$ quite sensitive to the forcing.

The transition to the high-forcing regime comes about when the stable equilibrated state described above becomes unstable and the asymptotic behavior is aperiodic. The role of the synoptic-scale waves in this regime is very similar to that in the low-forcing regime. The novelty is that the planetary wave is now also active. Its main role is to convert energy barotropically *from* the mean flow. This occurs in a rather intermittent fashion, giving the equilibrated state its fluctuating, chaotic character. The net effect of the planetary wave's barotropic conversion is to reduce zonal-mean horizontal shear and hence to lessen the role of the barotropic governor. The synoptic waves are therefore freer to transport heat, and the equilibrated temperature gradient is much less sensitive to forcing than in the low-forcing regime.

Differences between the CM and SM are due mainly to the fact that the CM is meridionally symmetric, while in the SM this symmetry is broken by the presence of the geometric curvature terms. Thus, at very low forcing, the CM exhibits a meridionally symmetric equilibrated state, though at slightly higher forcing the system goes through a bifurcation and there are actually two possible equilibrated states for a given forcing, the two being mirror images of each other about the channel center. In both states, the jet axis is shifted away from the channel center, either north- or southward. In regime C-II, the two states become unstable and the system jumps randomly between one and the other, leading to ''index cycle'' behavior of the jet. Conversely, regime S-I always features a single equilibrated state in which the jet axis is shifted north of the channel center. In regime S-II, the system oscillates around this northward-

confined state. There is also a quantitative difference between the two models in that eddy momentum flux convergence tends to be stronger in the SM, leading to a stronger barotropic governor there and generally higher sensitivity of $\Delta\theta_e$ to $\Delta\theta^*$.

In the following sections we describe these equilibration scenarios in greater detail.

### *a. The low-forcing regime*

#### 1) REGIME C-I

We illustrate this regime by taking the run at $\Delta\theta^* = 30$ K as an example. The time evolution, shown in Fig. 6, is initially dominated by wave 6, the most unstable wave, which goes through two life cycles between days 20 and 40. Single-wave life cycles such as this have been amply studied in the past (see, e.g., Feldstein and Held 1989). However, by day 40, waves 9 and 3 also reach finite amplitude; the system then goes through a rather intractable transient phase in which wave–wave interaction is important. This ends around day 80, by which time wave 3 has decayed to zero while waves 6 and 9 have reached steady finite amplitudes. At this point the system is essentially symmetric around the channel center, apart from a slight, periodic meridional oscillation. At lower forcing (e.g., at $\Delta\theta^* = 25$ K, not shown), this meridionally symmetric state is stable and persists for the duration of the run. In the present case, the symmetric state is not stable, and the jet gradually drifts northward; the final stable equilibrium is only reached after day 500. At higher forcings, the instability is stronger and the asymmetric final state is reached more quickly.

The structure of the equilibrated state is shown in Figs. 7a,c. Both waves are coaxial with the jet, and their momentum convergences are rather delicately counterbalanced. Presumably, the way this equilibrium works is that any tendency for wave 6, say, to change the structure of its momentum convergence will cause a change in the jet, which in turn will induce changes in wave 9's momentum convergence that exactly cancel those in wave 6. The small, high-frequency vacillation present in the equilibrated state (Fig. 6) is probably due to small mutual adjustments between the two waves. Note that the waves do not interact directly (wave–wave conversion is near zero for wave 6); they only ''see'' each other through the mediation of the zonal-mean flow. Note also that the momentum convergences do not sum to zero, since the waves must also balance the effects of forcing and dissipation.

Given the meridional symmetry of the governing equations, we may expect the existence of an analogous ''mirror image'' equilibrium. Indeed, this solution may easily be found numerically by taking a snapshot of the flow in the equilibrated state, reversing its latitude axis and using it as the initial state for a new integration. After a brief transient, the system settles into an equilibrium analogous to that above but with the jet pressed against the southern margin (not shown). Thus, in this regime, the model's phase space is split into (at least) two basins of attraction; the asymptotic behavior depends on which basin the initial state is in. In the $\Delta\theta^* = 70$ K run, the model ends up in the southern-confined state (Fig. 4a).

As is apparent from Fig. 3c, $\Delta\theta_e$ rises with $\Delta\theta^*$ throughout regime C-I (except at very low forcing, between $\Delta\theta^* = 20$ and 25 K; this range exhibits single-wave equilibration of a rather different nature to that described above). As forcing increases, the waves respond by raising their amplitude, which results in an increase in both baroclinic and barotropic conversion (Fig. 5c). The former acts to reduce mean temperature gradient, while the latter reduces the efficiency of the waves' baroclinic conversion and hence limits the reduction of the temperature gradient (the barotropic governor effect). Closer inspection of Fig. 3c shows that the rise in $\Delta\theta_e$ actually consists of two linear segments; comparison with Figs. 5g,i shows that these segments correspond to ranges in which waves 9 and 6 respectively dominate the baroclinic conversion. Thus it appears that each wave strikes up a balance between baroclinic conversion and barotropic governor effect such that $\Delta\theta_e$ is a fixed fraction of $\Delta\theta^*$. The magnitude of this fraction will depend on both zonal wavenumber and meridional wave structure, so it seems a difficult quantity to predict.

Note how different this equilibration is from the baroclinic adjustment–type behavior found by Pedlosky (1970) and Vallis (1988; see his Fig. 2). These authors both considered slightly supercritical initial states on the beta plane with uniform zonal-mean wind and found that after a few vacillation cycles the system settled into a state in which the initially most unstable wave reached finite, constant amplitude while the temperature gradient was reduced to its Hadley state critical value. In both those studies, however, the role of eddy momentum convergence was explicitly neglected, since the only mode

→

FIG. 5. Time-mean energetics of the equilibrated state as a function of $\Delta\theta^*$ in the CM (left-hand column) and SM (right-hand column). Top row shows zonal-mean APE (Az, upper thick solid line), zonal-mean KE (Kz, lower thick solid line), and total energy (APE + KE) of wave 3 (dashed line), wave 6 (thin solid line), and wave 9 (dotted line). The remaining panels show eddy energy conversion rates summed over all waves (second row) and separate contributions of wave 3 (third row), wave 6 (fourth row), and wave 9 (bottom row). Lines show conversion rates of zonal to eddy APE (Ca, thick solid) and KE (Ck, dotted), dissipation (Ds, dashed), and nonlinear transfer (thin solid). Errors bars as in Fig. 3.

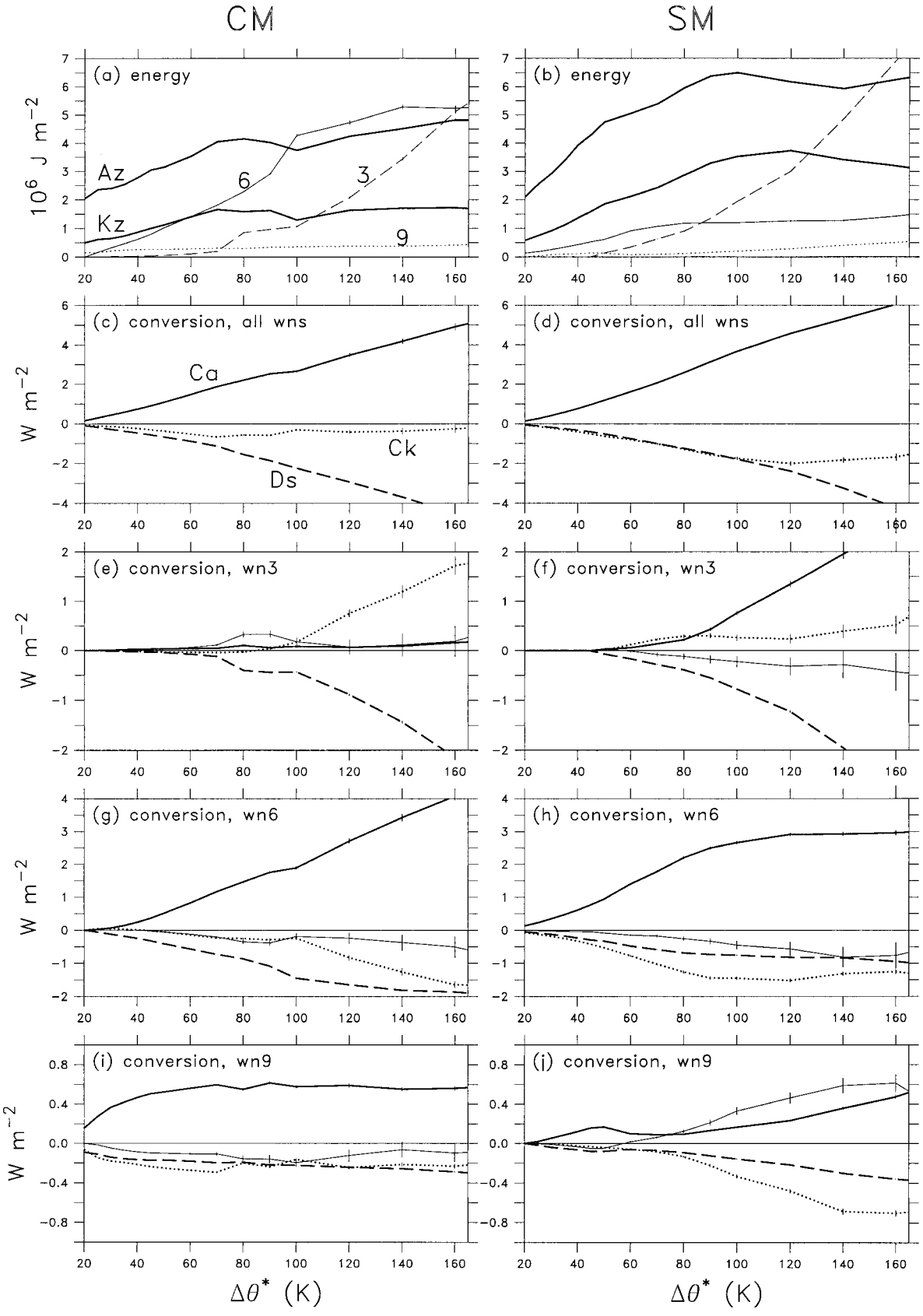
CM
SM
(a) energy
(b) energy
$10^6$ J m$^{-2}$
Az
Kz
6
3
9
(c) conversion, all wns
(d) conversion, all wns
W m$^{-2}$
Ca
Ck
Ds
(e) conversion, wn3
(f) conversion, wn3
(g) conversion, wn6
(h) conversion, wn6
(i) conversion, wn9
(j) conversion, wn9
$\Delta\theta^*$ (K)
$\Delta\theta^*$ (K)

that was allowed to grow was an eigenfunction of the Laplacian operator and hence was not meridionally tilted. When tilt *is* introduced in the growing wave, the barotropic governor plays an important role even in Cartesian geometry (Frisius 1998).

#### 2) REGIME S-I

We describe now the low-forcing regime on the sphere. We again take as an example the $\Delta\theta^* = 30$ K run. The time evolution (Fig. 8) is again initially dominated entirely by wave 6, which goes through a long sequence of life cycles featuring baroclinic growth and barotropic decay. Very similar behavior in a multilevel primitive equation model with a single active wave was found by Barnes and Young (1992). The wave's momentum flux convergence has an intrinsic northward bias due to sphericity (see section 3), and so each life cycle moves the jet farther and farther northward. We note that James et al. (1994) found similar slow northward propagation of zonal-mean flow anomalies in a multilevel primitive equation model, and Feldstein (1998) detected similar behavior in observational data. The eddy momentum fluxes eventually compress the jet against the rigid northern boundary, so that by day 100 we have an intense, narrow barotropic jet far north of the channel center. There is a region of weak easterlies on the southern flank that effectively confine the wave to the northern half of the channel. Momentum convergence is therefore weak in the southern half, and the radiative forcing is free to restore the westerlies there, in effect giving rise to a double-jet configuration. Even though the system is still supercritical, the strong meridional wind shear makes it harder and harder for the wave to extract energy baroclinically, so wave amplitude drops, reaching near zero around day 140. At this point the two regions of westerlies merge, the jet is restored to a shape similar to that in the Hadley state (but with lower temperature gradient) and a new chain of life cycles can begin. This new chain ends, by the same mechanism, at around day 300.

Now a new feature appears: the southern region of westerlies becomes unstable (in fact, linearly unstable as normal mode analysis reveals) to wave 9, whose amplitude and momentum convergence grow to finite size. The system then rapidly converges to an equilibrium state in which both waves have steady finite amplitude. The structure of this equilibrated state (Figs. 7b,d) is somewhat different from that in regime C-I. There are two distinct jets, a strong one at high latitude, associated with wave 6, and a weaker one at lower latitude, coaxial with wave 9. However, the momentum convergences of the two waves are again delicately balanced. The tendency for wave 6 to shift the southern flank of the strong jet northward is clearly offset by wave 9. Again, the two waves do not interact nonlinearly but only through the intermediation of the mean flow. This structure is maintained throughout regime S-I, though the intensity of the northern jet grows with $\Delta\theta^*$ while that of the southern jet weakens (Fig. 4b). We should note that attempts to find a southern-confined solution analogous to that found in regime C-I failed; indeed, the equations of motion are not meridionally symmetric, so we do not expect such a solution to exist. The system seems to have a single basin of attraction in this spherical case.

Turning to Fig. 3f, we see that $\Delta\theta_e$ rises linearly through regime S-I, consistent with the behavior found in C-I (note that wave 6 is dominant throughout S-I). However, the fractional reduction in temperature gradient is smaller than in C-I (i.e., $\Delta\theta_e$ rises more steeply). We may attribute this to the stronger barotropic jet spun up on the sphere (cf. Figs. 4a and 4b).

### *b. The high-forcing regime*

#### 1) REGIME C-II

As we saw above [section 5a(1)], in regime C-I the model's phase space is divided into two separate basins of attraction, corresponding to asymptotic states in which the jet is shifted north and south of the channel center. In regime C-II (forcings higher than $\Delta\theta^* = 70$ K), the two basins join up and the system can spontaneously transit from one solution to the other. This leads aperiodically to ''index cycle'' type behavior, in which the jet meanders meridionally. At first, transitions are rare (once every 1000 days or so at $\Delta\theta^* = 80$ K), but the transition frequency increases rapidly with forcing. In the range $\Delta\theta^* = 120$–160 K, the average residence time in each of the meridionally confined states is on the order of some tens of days.

Though wave 3 is not a dominant player in the time-mean energetics of this regime (see Figs. 3c and 5e), closer examination indicates that it does have an important role in inducing index cycle transitions. We will illustrate this with reference to the $\Delta\theta^* = 140$ K run. To focus on the index cycle behavior, we filter out the higher-frequency variability by running a 31-point Parzen window through the time series. Results are shown in Fig. 9. We can clearly see the zonal-mean wind os-

→

FIG. 6. Time series of the $\Delta\theta^* = 30$ K CM run, representative of regime C-I. Left (right) column shows days 1–120 (120–1000). Top row: Time series of the barotropic component of the zonal-mean wind. Contour interval is 2 m s$^{-1}$. Zero contour is darkened and negative contours dashed. Second row: Zonal-mean APE (upper thick solid line), zonal-mean KE (lower thick solid line), and total energy (APE + KE) of wave 3 (dashed line), wave 6 (thin solid line), and wave 9 (dotted line). Remaining panels show energy conversion rates of (third row) wave 6 and (bottom row) wave 9; lines show conversion rates of zonal to eddy APE (thick solid line) and KE (dotted line), dissipation (dashed line), and nonlinear transfer (thin solid line). Note the different *y*-axis scales in the left and right columns.

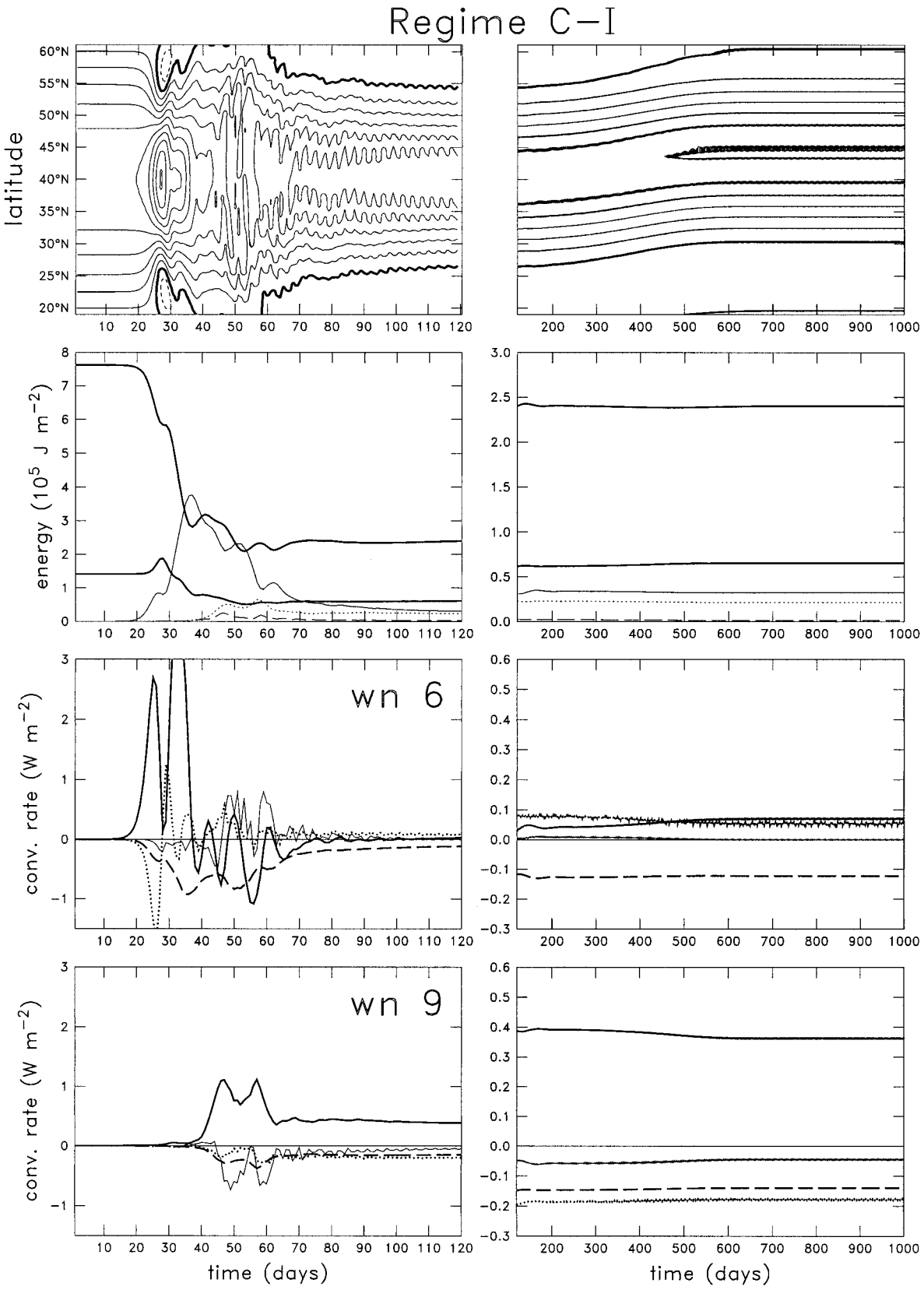
Regime C–I
latitude
60°N
55°N
50°N
45°N
40°N
35°N
30°N
25°N
20°N
energy ($10^5$ J m$^{-2}$)
wn 6
wn 9
conv. rate (W m$^{-2}$)
time (days)
10 20 30 40 50 60 70 80 90 100 110 120
200 300 400 500 600 700 800 900 1000

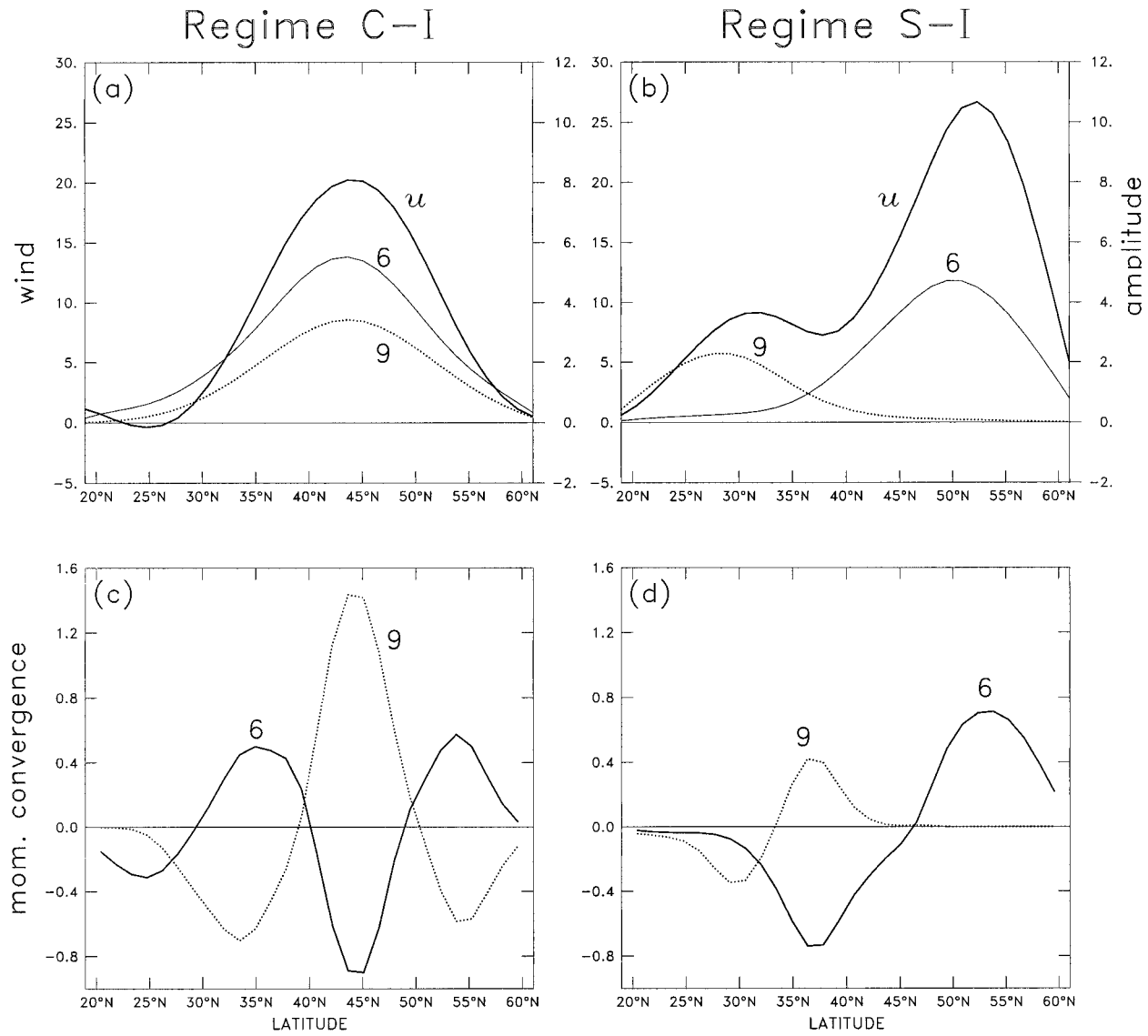


FIG. 7. The equilibrated state of the $\Delta\theta^* = 30$ K run in the CM (left column) and SM (right column). Top row: barotropic zonal-mean wind ($u$, thick solid), and streamfunction amplitudes of wave 6 (thin solid line) and wave 9 (dotted line). Left axis refers to wind (units m $s^{-1}$), right axis to amplitude (unit $10^6$ $m^2$ $s^{-1}$). Bottom row: momentum flux convergence of wave 6 (solid line) and wave 9 (dotted line), unit m $s^{-1}$ $day^{-1}$.

cillating between configurations with a strong, northward- or southward-confined westerly jet; in between are transition states with much weaker meridional wind shear. The meridionally confined events coincide with peaks in the zonal-mean KE and APE (Fig. 9b). The energy of wave 6 (wave 3) peaks shortly before (after) each meridionally confined event.

Examination of the waves' energetics (Figs. 9c,d) gives some indication as to the underlying dynamics. We note the following: at the beginning of each meridionally confined event, the rate at which wave 6 feeds KE to the mean flow increases sharply (viz., days 370, 430, 500); wave 6's baroclinic conversion rate dips to a minimum during each event; wave 3's barotropic and baroclinic conversion rates both increase during each event, peaking around the time when the system begins to exit the confined state. We may coherently interpret this behavior by assuming that each event is initiated by wave 6, whose momentum convergence attempts to push the system into a meridionally confined state. The intense meridional wind shears thus generated reduce wave 6's own baroclinic conversion rate through the barotropic governor mechanism. Wave 6 thus experiences a net energy loss and its total energy drops. The reduced baroclinic conversion allows the radiative forcing to drive up the zonal-mean APE, which increases together with the KE. At this point, wave 3 comes into play, with an effect opposite to that of wave 6: it grows

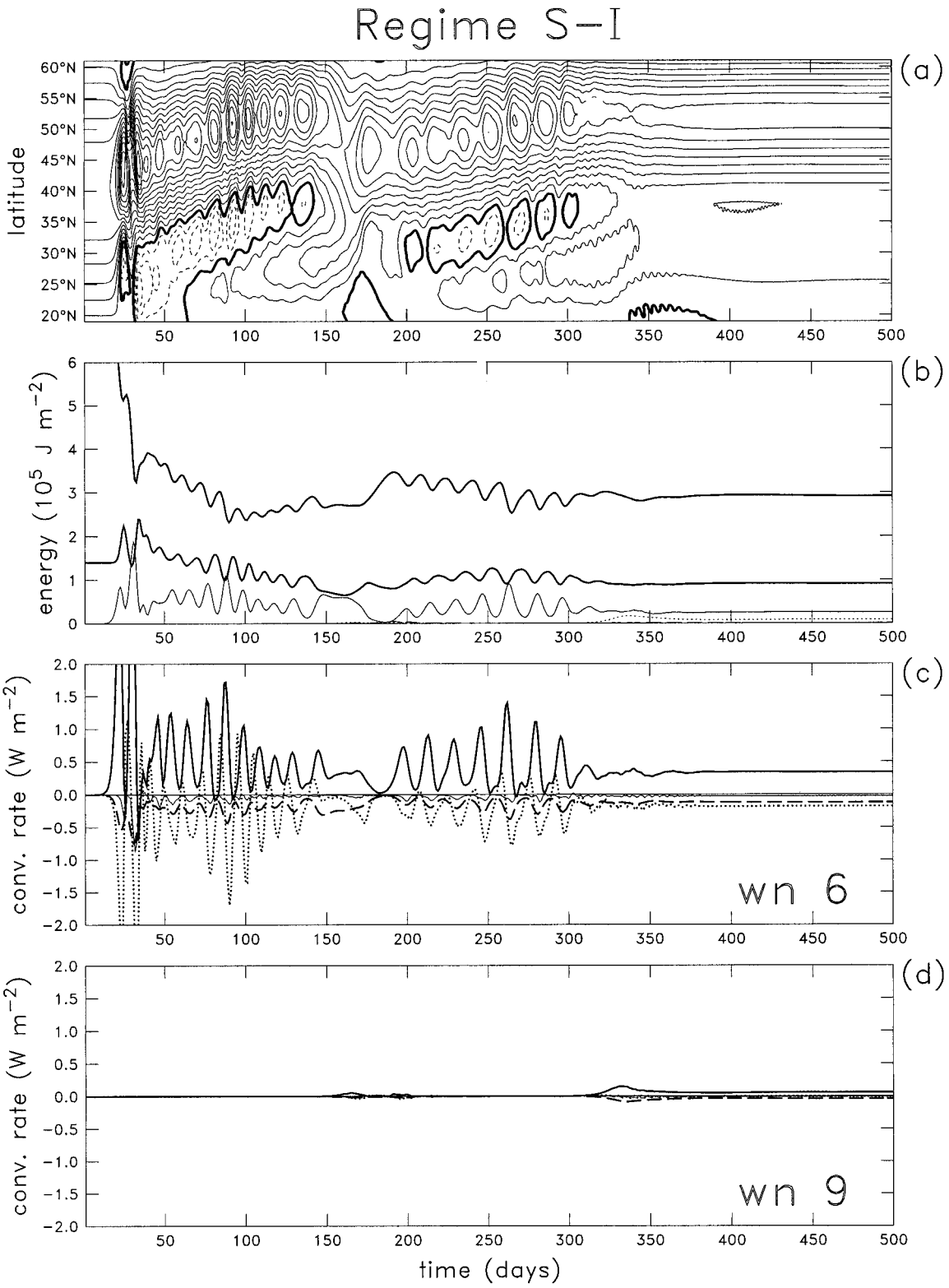


FIG. 8. As in Fig. 6 but for the first 500 days of the $\Delta\theta^* = 30$ K SM run, representative of regime S-I.

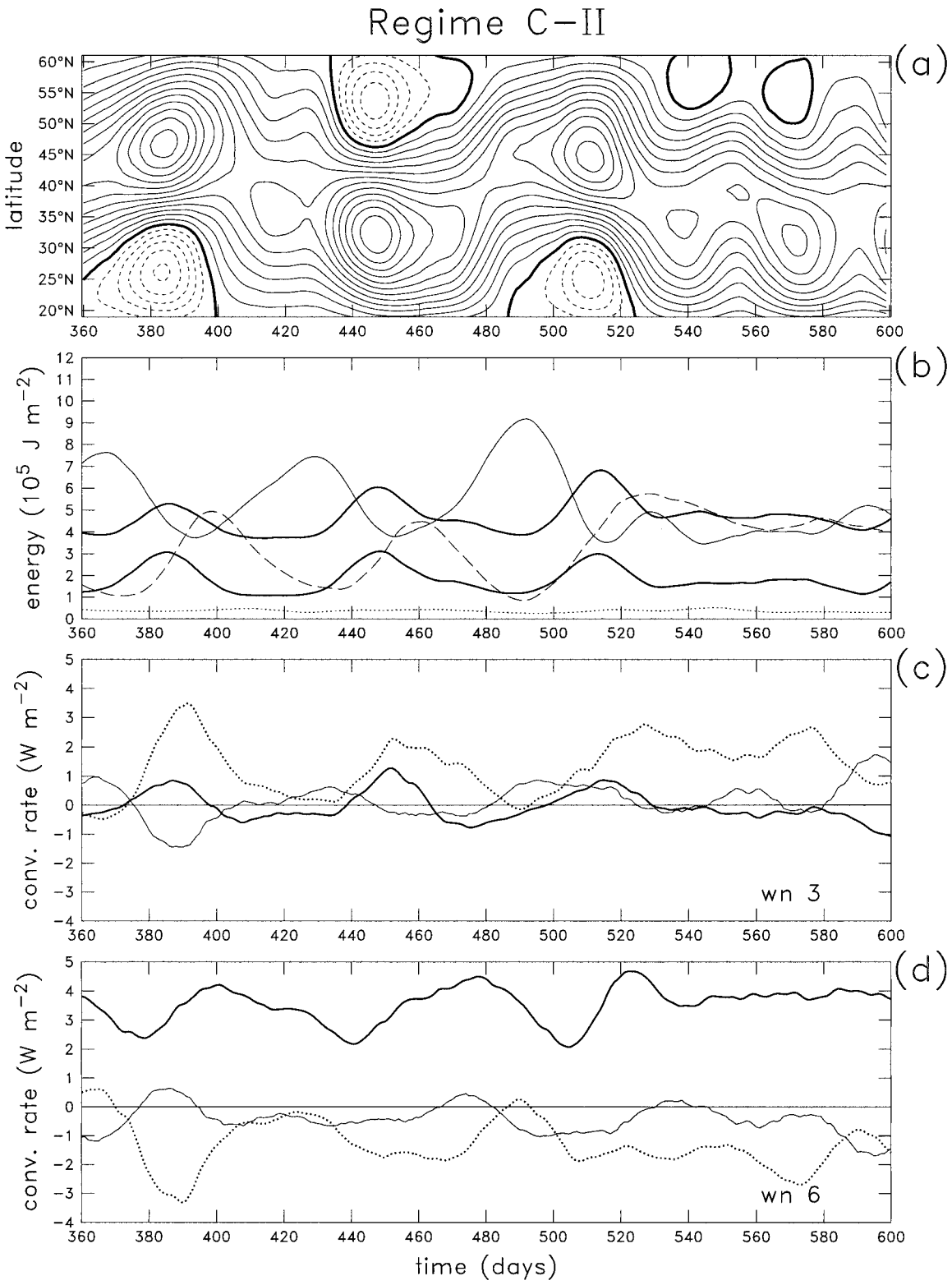


FIG. 9. As in Fig. 6 but for 240 days of the $\Delta\theta^* = 140$ K CM run, representative of regime C-II. All time series are smoothed using a 31-point Parzen window running mean. Dissipation has been omitted from (c) and (d) to avoid clutter.

mainly by barotropic conversion, reducing the meridional shear and eventually driving the system out of the meridionally confined state.

The discussion above suggests a scenario where the meridionally confined states are still attracting to wave 6 but are unstable to wave 3; the index cycle behavior follows from the interplay of the two waves. We note that the wave 3 instability is most likely a finite-amplitude effect: though linear instability analysis between days 380 and 390 (for instance) does reveal unstable wavenumber 3 modes, their growth rate is slow and there is not much evidence of barotropic instability. The role of wave–wave interactions in this picture is not at present clear to us. Net energy exchange between the two waves does not appear to be well synchronized with the index cycle (note that during the day 360–400 event, wave 3 is giving energy to wave 6, and vice versa during the day 500–520 event). Figures 5e,g indicate, however, that in the long-term average wave–wave energy exchange is a net sink for wave 6 and a net source for wave 3.

Finally, we attempt to account for the behavior of the $\Delta\theta_e$ curve in this regime. We note that the zonal-mean APE (and hence also the cross-channel temperature gradient) is always lower during transitions than in the meridionally confined states, while the average value of the APE in both the confined and the transition states rises steadily with $\Delta\theta^*$. In the low-forcing end of this regime, the statistics are dominated by the fact that the residence time in confined states is decreasing rapidly, so that the system spends more and more time in states with low temperature gradient. Thus $\Delta\theta_e$ drops. At higher forcing, on the other hand, the residence time decreases only slowly, and thus the dominant effect is the net rise in the temperature gradient, giving the slow rise in $\Delta\theta_e$ observed after $\Delta\theta^* = 100$ K. Overall, $\Delta\theta_e$ is much less sensitive to $\Delta\theta^*$ in this regime than in C-I, and this difference appears to be due to the disruptive effect of wave 3, which pushes the system away from states in which the barotropic governor is strong.

#### 2) REGIME S-II

We saw above that regime S-I exhibits a single stable asymptotic state. After $\Delta\theta^* = 50$ K, this state becomes unstable, in a manner analogous to that observed in regime C-II. There is, however, no index cycle behavior, since there is no southern-confined state for the system to transit to. Rather, the model oscillates aperiodically about the northern-confined state, deviating farther and more frequently from it as forcing is increased.

We will document these facts with reference to the case $\Delta\theta^* = 60$ K (Fig. 10). The upper panel shows the barotropic jet, which is again much narrower and farther north than in the Hadley state. Its maximum intensity fluctuates with a timescale of some tens of days; cross sections would show it oscillating between a very narrow, intense configuration and a broader, less intense one. Figure 10b shows that wave 3 activity comes in bursts, which coincide with the minima in barotropic jet intensity. The bursts also precede longer bursts of wave 6 activity.

The waves' energetics (Figs. 10c,d) give some indication of the mechanism underlying these bursts. First, note that nonlinear transfer, though large in absolute value, changes sign very rapidly. Apparently, energy is shuttling back and forth between waves 3 and 6, so quickly that dissipative effects have no time to intervene; for this reason, the process is conservative and there is no net transfer. Now consider the situation at day 745, just before the first wave 3 burst. A linear stability study at this instant (not shown) reveals that the zonal-mean flow is unstable; the most unstable normal mode has wave 3 and is a mixed barotropic–baroclinic instability. Consistently, the energetics (Fig. 10c) show wave 3 gaining energy both baroclinically and barotropically. At day 749, wave 3 receives a large amount of energy from wave 6 by nonlinear transfer; this ''kick'' speeds up linear conversion, and wave 3 energy grows quickly. By day 753, barotropic shear has been significantly reduced and the mean flow is stable to wave 3, whose energy now decays. However, the barotropic governor is now less active and so wave 6 is free to grow by baroclinic conversion. Eventually, by day 757, wave 6 spins up a sufficiently intense barotropic jet to neutralize itself and it begins to decay. The whole process then starts again around day 765. Note that wave 3 bursts occur when nonlinear transfer is synchronized with linear conversion; it does not seem that nonlinear transfer can *cause* wave 3 to extract energy from the mean flow.

Since wave 3 is actively reducing the meridional wind shear and hence the barotropic governor, we expect $\Delta\theta_e$ to be less sensitive to $\Delta\theta^*$ in S-II than in S-I; this is indeed the case, as Fig. 3f shows. We note also that after $\Delta\theta^* = 80$ K, wave 6 saturates (i.e., its amplitude ceases to grow with the forcing; see Fig. 5b). Since the barotropic jet is chiefly maintained by wave 6 (with a smaller contribution from wave 9; see Figs. 5h,j), this means that after $\Delta\theta^* = 80$ K the barotropic governor essentially stops growing; $\Delta\theta_e$ then becomes almost independent of $\Delta\theta^*$.

## 6. Conclusions

We summarize our main conclusions as follows.

1) The inclusion of small symmetry-breaking terms in the equations of motion can lead to qualitative differences in the finite-amplitude equilibration, even when several waves are present. This confirms and expands the results of Nakamura (1993), who studied the equilibration of a single wave.
2) The crucial terms are those reflecting the curved geometry (convergence of the meridians) rather than

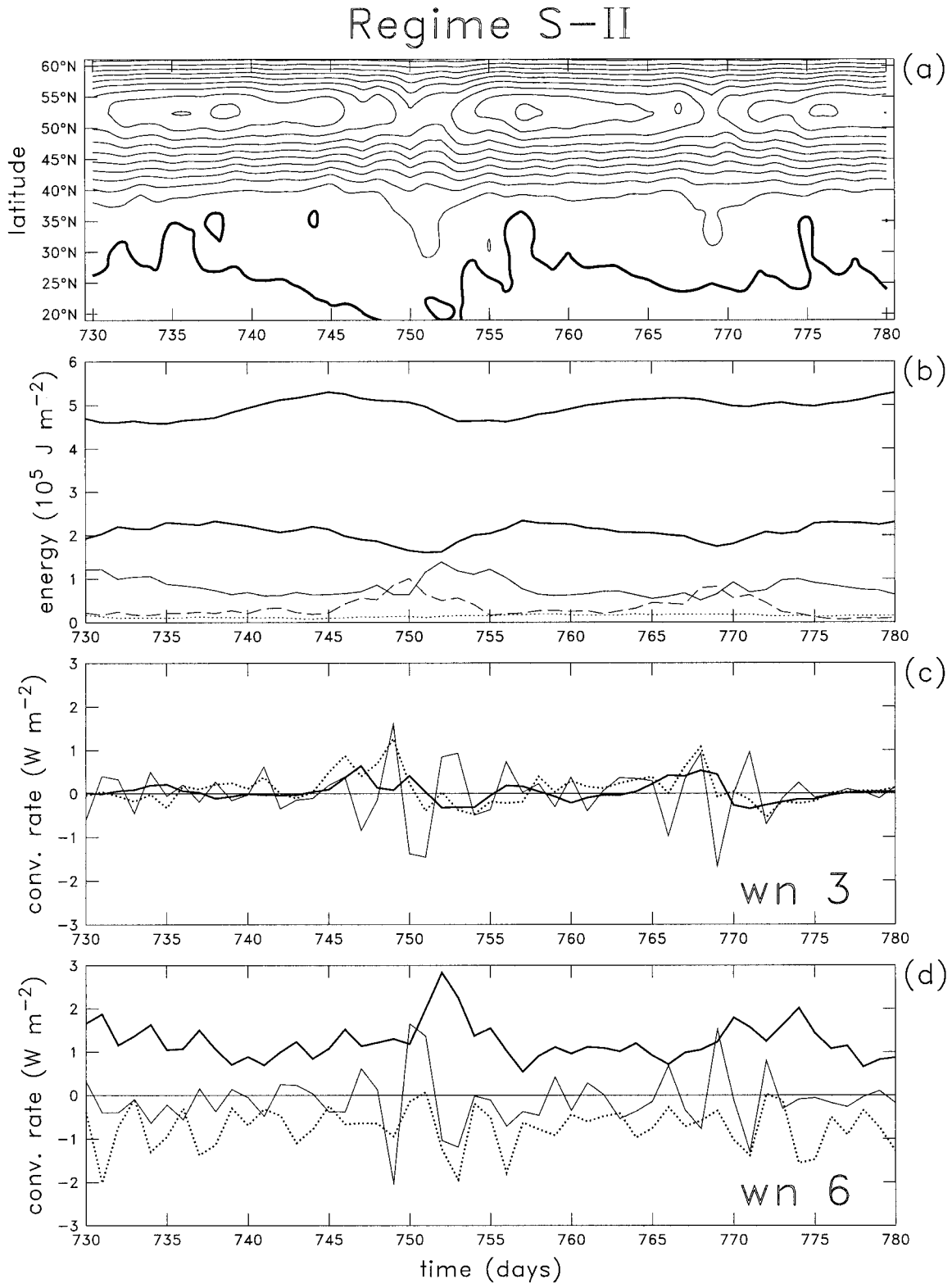


FIG. 10. As in Fig. 6 but for a 40-day segment of the $\Delta\theta^* = 60$ K SM run, representative of regime S-II. Contour interval in (a) is 3 m s$^{-1}$. Dissipation has been omitted from (c) and (d) to avoid clutter.

the meridional variation of $\beta$: indeed, the CM and VBM behave almost identically.

3) In both Cartesian and spherical geometry, eddy fluxes can significantly distort the shape of the equilibrated zonal-mean flow. This means that it is difficult or even impossible to predict the equilibrated temperature gradient in terms of the Hadley state critical gradients. In the model we have studied, the relative error implied in such a prediction is around 25% (50%) in Cartesian (spherical) geometry.
4) The barotropic governor effect is active in both Cartesian and curved geometry. The effect of the barotropic governor is to make the equilibrated temperature gradient sensitive to the forcing temperature gradient. In the cases considered here, this is chiefly observed at low forcing. When the forcing is high enough, the planetary wave can feed off the barotropic jet's KE and hence weaken the barotropic governor, making $\Delta\theta_e$ much less sensitive to $\Delta\theta^*$.
5) The barotropic governor effect is is stronger in spherical geometry, apparently because the systematic northward bias of the momentum fluxes induced by the curvature terms produces a stronger meridionally confined jet. Zhou and Stone (1993) noted higher sensitivity of the equilibrated temperature gradient to forcing in their spherical geometry study than in the $\beta$-channel study of Stone and Branscome (1992).
6) The equilibration is dominated by wave–zonal flow interaction, with wave–wave interaction playing a marginal [though sometimes subtle, as in section 5b(2)] role. Time averaged and summed over all waves, baroclinic conversion has much greater magnitude and opposite sign to barotropic conversion. The observational study of Randel and Stanford (1985a) came to the same conclusion, at least with regard to the Southern Hemisphere summer.

We note again the many restrictive assumptions made in the present study. Realism is compromised, among other things, by the presence of sidewalls, which play a crucial role in confining the jet and bringing the barotropic governor into play. Also, the presence of planetary-scale topographic features (absent here but present in reality) could bring the planetary wave into action even at low forcing, possibly weakening the barotropic governor. A third question is what will happen when a wider spectrum of waves is allowed to participate in the equilibration. We are currently studying these problems in the more realistic context of a primitive equation model.

*Acknowledgments.* Discussions with Wendy Welch and the comments of two anonymous reviewers helped improve the presentation of the material in this paper. AS acknowledges support from the European Commission under Contract ENV4-CT960344 and from Agenzia Spaziale Italiana (ASI). RC was supported by the European Commission through Contract ENV4-CT96-5045 and by the Dansk Grundforskningsfond. Graphics were produced with Ferret freely available software (http://ferret.wrc.noaa.gov).

## REFERENCES

Baines, P. G., and J. S. Frederiksen, 1978: Baroclinic instability on a sphere in two-layer models. *Quart. J. Roy. Meteor. Soc.,* **104,** 45–68.

Balasubramanian, G., and S. T. Garner, 1997: The role of momentum fluxes in shaping the life cycle of baroclinic waves. *J. Atmos. Sci.,* **54,** 510–533.

Barnes, J. R., and R. E. Young, 1992: Nonlinear baroclinic instability on the sphere: Multiple life cycles with surface drag and thermal damping. *J. Atmos. Sci.,* **49,** 861–878.

Bordi, I., and A. Sutera, 1998: On baroclinic adjustment of a radiative-convective atmosphere. *Ann. Geofis.,* **41,** 643–652.

Cehelsky, P., and K. K. Tung, 1991: Nonlinear baroclinic adjustment. *J. Atmos. Sci.,* **48,** 1930–1947.

Charney, J. G., and M. Stern, 1962: On the stability of internal baroclinic jets in a rotating atmosphere. *J. Atmos. Sci.,* **19,** 159–172.

Dong, B. W., and I. N. James, 1997: The effect of barotropic shear on baroclinic instability. 1. Normal mode problem. *Dyn. Atmos. Oceans,* **25,** 143–167.

Edmon, H. J., Jr., B. J. Hoskins, and M. E. McIntyre, 1980: Eliassen–Palm cross sections for the troposphere. *J. Atmos. Sci.,* **37,** 2600–2616.

Feldstein, S. B., 1998: An observational study of the intraseasonal poleward propagation of zonal mean flow anomalies. *J. Atmos. Sci.,* **55,** 2516–2529.

——, and I. M. Held, 1989: Barotropic decay of baroclinic waves in a two-layer beta-plane model. *J. Atmos. Sci.,* **46,** 3416–3430.

Frisius, T., 1998: A mechanism for the barotropic equilibration of baroclinic waves. *J. Atmos. Sci.,* **55,** 2918–2936.

Gutowski, W. J., 1985: Baroclinic adjustment and midlatitude temperature profiles. *J. Atmos. Sci.,* **42,** 1733–1745.

Held, I. M., 1978: The vertical scale of an unstable wave and its importance for eddy heat flux parameterizations. *J. Atmos. Sci.,* **35,** 572–576.

——, 1999: The macroturbulence of the troposphere. *Tellus,* **51A,** 59–70.

James, I. N., 1987: Suppression of baroclinic instability in horizontally sheared flows. *J. Atmos. Sci.,* **44,** 3710–3720.

——, and L. J. Gray, 1986: Concerning the effect of surface drag on the circulation of a baroclinic planetary atmosphere. *Quart. J. Roy. Meteor. Soc.,* **112,** 1231–1250.

James, P. M., K. Fraedrich, and I. N. James, 1994: Wave–zonal-flow interaction and ultra-low-frequency variability in a simplified global circulation model. *Quart. J. Roy. Meteor. Soc.,* **120,** 1045–1067.

Lindzen, R. S., 1993: Baroclinic neutrality and the tropopause. *J. Atmos. Sci.,* **50,** 1148– 1151.

Lorenz, E. N., 1960: Energy and numerical weather prediction. *Tellus,* **12,** 364–373.

Mak, M., 1991: Influences of the Earth's sphericity in the quasigeostrophic theory. *J. Meteor. Soc. Japan,* **69,** 37–65.

Manabe, S., and R. F. Strickler, 1964: On the thermal equilibrium of the atmosphere with a convective adjustment. *J. Atmos. Sci.,* **21,** 316–385.

Nakamura, N., 1993: Momentum flux, flow symmetry, and the nonlinear barotropic governor. *J. Atmos. Sci.,* **50,** 2159–2179.

Pedlosky, J., 1970: Finite-amplitude baroclinic waves. *J. Atmos. Sci.,* **27,** 15–30.

Phillips, N. A., 1954: Energy transformations and meridional circulations associated with simple baroclinic waves in a two level, quasi-geostrophic model. *Tellus,* **6,** 273–286.

Randel, W. J., and J. L. Stanford, 1985a: An observational study of medium-scale wave dynamics in the Southern Hemisphere sum-

mer. Part I: Wave structure and energetics. *J. Atmos. Sci.,* **42,** 1172–1187.

——, and ——, 1985b: The observed life cycle of a baroclinic instability. *J. Atmos. Sci.,* **42,** 1364–1373.

Salmon, R. S., 1980: Baroclinic instability and geostrophic turbulence. *Geophys. Astrophys. Fluid Dyn.,* **15,** 167–211.

Simmons, A. J., and B. J. Hoskins, 1978: The life cycles of some nonlinear baroclinic waves. *J. Atmos. Sci.,* **35,** 414–432.

Stone, P. H., 1978: Baroclinic adjustment. *J. Atmos. Sci.,* **35,** 561–571.

——, and L. Branscome, 1992: Diabatically forced, nearly inviscid eddy regimes. *J. Atmos. Sci.,* **49,** 355–367.

Thuburn, J., and G. C. Craig, 1997: GCM tests of theories for the height of the tropopause. *J. Atmos. Sci.,* **54,** 869–882.

Vallis, G. K., 1988: Numerical studies of eddy transport properties in eddy resolving and parametrized models. *Quart. J. Roy. Meteor. Soc.,* **114,** 183–204.

Welch, W. T., and K. K. Tung, 1998a: Nonlinear baroclinic adjustment and wavenumber selection in a simple case. *J. Atmos. Sci.,* **55,** 1285–1302.

——, and ——, 1998b: On the equilibrium spectrum of transient waves in the atmosphere. *J. Atmos. Sci.,* **55,** 2833–2851.

Whitaker, J. S., and C. Snyder, 1993: The effects of spherical geometry on the evolution of baroclinic waves. *J. Atmos. Sci.,* **50,** 597–612.

Zhou, S., and P. H. Stone, 1993: The role of large-scale eddies in the climate equilibrium. Part I: Fixed static stability. *J. Climate,* **6,** 985–1001.